Check for updates

JGR Atmospheres

RESEARCH ARTICLE
10.1029/2021JD036359

Investigation of Tropical Cyclone Wind Models With Application to Storm Tide Simulations

Shuai Wang[1], **Ning Lin**[1], **and Avantika Gori**[1]

[1]Department of Civil and Environmental Engineering, Princeton University, Princeton, NJ, USA

Key Points:

- A physics-based complete wind profile model shows a better capability of depicting the TC symmetrical wind than the Holland wind model
- A background-wind-based model can capture the TC wind asymmetry well with computational efficiency
- The physics-based wind profile coupled with the background-wind model may be a better way of forcing TC-induced storm tide simulations

Correspondence to:
S. Wang,
shuai.wang@princeton.edu

Citation:
Wang, S., Lin, N., & Gori, A. (2022). Investigation of tropical cyclone wind models with application to storm tide simulations. *Journal of Geophysical Research: Atmospheres*, *127*, e2021JD036359. https://doi.org/10.1029/2021JD036359

Received 14 DEC 2021
Accepted 25 AUG 2022

Author Contributions:
Conceptualization: Shuai Wang, Ning Lin
Formal analysis: Shuai Wang, Avantika Gori
Funding acquisition: Ning Lin
Methodology: Shuai Wang
Visualization: Shuai Wang
Writing – original draft: Shuai Wang
Writing – review & editing: Shuai Wang, Ning Lin, Avantika Gori

© 2022. The Authors.
This is an open access article under the terms of the Creative Commons Attribution License, which permits use, distribution and reproduction in any medium, provided the original work is properly cited.

Abstract The hazards induced by tropical cyclones (TCs), for example, high winds, extreme precipitation, and storm tides, are closely related to the TC surface wind field. Parametric models for TC surface wind distribution have been widely used for hazards and risk analysis due to their simplicity and efficiency in application. Here we revisit the parametric modeling of TC wind fields, including the symmetrical and asymmetrical components, and its applications in storm tide modeling in the North Atlantic. The asymmetrical wind field has been related to TC motion and vertical wind shear; however, we find that a simple and empirical background-wind model, based solely on a rotation and scaling of the TC motion vector, can largely capture the observed surface wind asymmetry. The implicit inclusion of the wind shear effect can be understood with the climatological relationship between the general TC motion and wind shear directions during hurricane seasons. For the symmetric wind field, the widely used Holland wind profile is chosen as a benchmark model, and we find that a physics-based complete wind profile model connecting the inner core and outer region performs superiorly compared to a wind analysis data set. When used as wind forcing for storm tide simulations, the physics-based complete wind profile integrated with the background-wind asymmetry model can reproduce the observed storm tides with lower errors than the often-used Holland model coupled with a translation-speed-based method.

Plain Language Summary The socioeconomic repercussions incurred by tropical cyclones (TC) are closely related to the TC surface wind distribution. Considering the symmetrical feature of mature TCs' structure, parametric wind profile models—depicting the mean surface wind speed at various radial distances to the TC center—have been widely applied in TC-related hazard and risk assessment, mainly due to their simple mathematical expression and computational efficiency in application. In this study, we show that a physics-based complete wind profile model, connecting the inner and outer TC cores, performs superiorly compared to the widely used Holland wind model when validated against a wind analysis data set. We also find that a simple background wind model can well capture the observed surface wind asymmetry. When used as wind forcing for storm tide simulations, the complete wind profile integrated with the background-wind model can reproduce the observed storm tides along the U.S. East and Gulf coasts with lower errors than the often-used Holland model coupled with a translation-speed-based method.

1. Introduction

Tropical cyclones (TCs) pose the greatest threat to lives and economy along the US coasts (Klotzbach et al., 2018; Pielke et al., 2008; Rappaport, 2014). The main impacts of TCs at landfall include high winds, intense precipitation with flash floods, storm tide inundation, and resulting coastal infrastructure failure (Gori, Lin, & Smith, 2020; Lin, Smith, et al., 2010; Marsooli et al., 2019; Yin et al., 2020). All these three impacts can be related to TC surface winds. Extreme winds can be directly calculated from TC surface winds (Xu et al., 2020). The wind impact can be also represented by the integrated kinetic energy calculated with the surface wind field (Powell & Reinhold, 2007; S. Wang & Toumi, 2021), which shows a high correlation with the economic cost at landfall in the U.S (S. Wang & Toumi, 2016). Rainfall intensity can be estimated with the surface wind distribution and mass conservation in a simple TC rainfall model (Lu et al., 2018; Xi et al., 2020; Zhu et al., 2013). This rainfall model has also been used recently for TC-related risk assessment (Emanuel, 2017b; Gori et al., 2022; Gori, Lin, & Xi, 2020). Storm tide can be decomposed as a combination of astronomical tide and storm surge, and the surge is challenging to assess due to the nonlinear interactions between the atmosphere, ocean and bottom topography of coastal shelfs (Anthes, 1982). Storm surge is associated with the ocean depth/shelf width and TC pressure and wind conditions (Harris, 1963; Irish et al., 2008; Joyce et al., 2019; Lin, Emanuel, et al., 2010; Marsooli &

21698996, 2022, 17, Downloaded from https://agupubs.onlinelibrary.wiley.com/doi/10.1029/2021JD036359, Wiley Online Library on [20/12/2023]. See the Terms and Conditions (https://onlinelibrary.wiley.com/terms-and-conditions) on Wiley Online Library for rules of use; OA articles are governed by the applicable Creative Commons License

Lin, 2018; Rego & Li, 2009; Weisberg & Zheng, 2006). With proximity to a wide continental shelf the surge magnitude is primarily driven by TC surface winds (Wong & Toumi, 2016).

The TC surface wind field can be decomposed into symmetrical and asymmetrical components. The radial variation of the symmetrical wind component is determined by the nature of a vortex in a viscous fluid, which can be approximately regarded as a Rankine vortex, with the wind speed increasing from the vortex center and then decreasing in outer radii (Depperman, 1947). The wind asymmetry is considered to be caused by a background wind field (Lin & Chavas, 2012). The mean background wind effect is largely reflected by TC motions. However, the TC motion does not superpose on the symmetric wind component in a linear manner, and Shapiro (1983) showed in theory that the location of maximum surface wind related to TC motion rotates to the down-motion-right quadrant. Wind asymmetry can also be caused by vertical wind shears in the ambient environment, with a preferential wavenumber-1 maximum storm motion-relative surface wind asymmetry located down-shear-left in the West Pacific (Ueno & Bessho, 2011) and North Atlantic (Klotz & Jiang, 2017).

Despite the importance of TC surface winds to hazards, to date it is still hardly possible to observe a timely, accurate and complete wind field for all the TCs. Alternatively, some features of surface wind field are routinely reported, such as the speed and radius of maximum wind and some sparse outer wind radii. To overcome this obstacle, parametric TC wind models have been developed for the symmetrical wind component (Depperman, 1947; Emanuel & Rotunno, 2011; S. Wang et al., 2015; Willoughby et al., 2006), and asymmetrical wind component (Chang et al., 2020; Lin & Chavas, 2012; Olfateh et al., 2017). The regional climate models, for example, the Weather Research and Forecasting Model, can generate complete wind fields for TC forecasts (Bernardet et al., 2015; Gopalakrishnan et al., 2011; Zhang et al., 2016) and hindcasts (Lin, Smith, et al., 2010), but a detailed description of the atmospheric initial and boundary conditions are required, which is hardly met when assessing the TC-related risk especially in future climate scenarios. The wind field uncertainty caused by using the inherent small-scale parameterizations in regional climate models has also to be considered. By contrast, the wind profile model can conveniently produce a wind distribution with only a few key TC features from the synthetic TC tracks downscaled from reanalysis and climate projections (Emanuel, 2017a; Jing & Lin, 2020; Lee et al., 2020). Thus, the parametric TC wind model is still an indispensable tool for the risk analysis related to TC wind fields.

In parametric TC wind analysis, the symmetrical component of the surface wind field can be modeled with a wind profile fitted to storm parameters (mainly the speed and radial position of maximum wind). The Holland model (Holland, 1980, hereafter H80) is arguably the most widely used TC surface wind profile model for the symmetrical wind modeling. The H80 model was established based on the gradient wind balance and a statistically assumed rectangular hyperbolas shape of pressure field. For a better complete wind field representation, a revised H80 model was proposed to incorporate in an outer wind radius (Holland et al., 2010). However, the outer wind radius still lacks accuracy in operational forecasts (Landsea & Franklin, 2013a, 2013b; Sampson et al., 2018), has much shorter historical records compared to TC intensities [for example, only back to 1988 in the North Atlantic (Demuth et al., 2006)], and is not estimated for synthetic TC tracks downscaled from reanalysis or climate models (Emanuel et al., 2008; Jing & Lin, 2020; Lee et al., 2018). These issues bring difficulty to implement the revised Holland model for TC historical analyses, operational forecasts, and future projections.

An alternative wind profile model including both the inner and outer wind distributions was derived by Chavas et al. (2015, hereafter CLE15). The CLE15 model is a physics-based model combining two existing TC theories for inner- and outer-core wind changes, respectively (Emanuel, 2004; Emanuel & Rotunno, 2011). The two solutions are connected at a merge point where the angular momentum and its radial derivative are mathematically continuous. The CLE15 model can simulate a complete wind profile with the TC features in the inner core (i.e., maximum wind and radius of maximum wind) as used by other wind profile models, although it can also simulate the wind profile using an outer wind radius in place of the radius of maximum wind (Chavas & Lin, 2016). It has been shown that the CLE15 model provides a credible physical solution for the complete TC wind field (Chavas & Lin, 2016). However, the CLE15 model has not been directly compared with other wind profile models.

The radial wind profile is a good approximation to the complete wind field for zero order; however, the asymmetric wind component cannot be ignored, especially when considering its impact on storm surge (Wang et al., 2021). A simple approach for the asymmetrical wind modeling was introduced by Lin and Chavas (2012, hereafter LC12) by adding in a simple empirically estimated surface background wind vector onto the symmetric wind profile. They showed that based on observations the surface background wind vector can be estimated based on the TC motion vector with a reduction factor of 0.6 on the translational speed and counter-clockwise rotation

21698996, 2022, 17, Downloaded from https://agupubs.onlinelibrary.wiley.com/doi/10.1029/2021JD036359, Wiley Online Library on [20/12/2023]. See the Terms and Conditions (https://onlinelibrary.wiley.com/terms-and-conditions) on Wiley Online Library for rules of use; OA articles are governed by the applicable Creative Commons License

of about 20°. A more sophisticated method to introduce wind asymmetry was recently developed by including the vertical wind shear as an additional factor (Chang et al., 2020, hereafter CAE20). The amplitudes and phases of the asymmetry in CAE20 are empirical functions of the speeds of TC motion and wind shear with eight fitted parameters. CAE20 found a large improvement of their wind model performance by considering the translation vector and wavenumber-1 asymmetry resulting from translation. However, the performance improvement is only marginal by including the wavenumber-1 information resulting from shear. Both LC12 and CAE20 need to be coupled with a symmetric wind profile, and it is unknown which model is a better choice for the complete wind field modeling.

This study will evaluate some of these parametric TC wind models for the asymmetrical and symmetrical wind simulations and make a recommendation for wind forcing for storm tide modeling. There are three objectives in this study. First, we aim to revisit the ability of the CLE15 model to represent the observed symmetric wind profile, using the H80 model as a benchmark (Section 3). Second, we will evaluate different ways (i.e., LC12 and CAE20) of introducing wind asymmetry in comparison with a wind analysis data set (Section 4). Third, the H80 and CLE15 models coupled with different wind asymmetry approaches will be examined as the wind forcing for historical storm tide simulation of the U.S. landfalling TCs over 1988–2020 (132 storms, Section 5). The last section will discuss and summarize the key findings and make a recommendation of complete TC surface wind models for storm surge simulations.

2. Methods

2.1. Atmospheric Data Sets

The TC wind field in the North Atlantic is taken from the HWind analysis data set (Powell et al., 1998a, 1998b) for the period of 1998–2013. The horizontal grid spacing of HWind is 6 km with a coverage of 1000 ×1,000 km^2 square of each wind snapshot. HWind snapshots provide 1 min sustained winds derived by processing remotely sensed and in situ observations and assimilation. The wind uncertainty of HWind is approximately 6% near the eyewall and 13% near the radius of gale force wind (Dinapoli et al., 2012). In comparison to other recently developed wind product, for example, Real-Time Mesoscale Analysis/Unrestricted Mesoscale Analysis (TRMA/URMA), HWind is not based on the state-of-the-art data assimilation technique. However, the HWind analysis, which includes reconnaissance data, is arguably still the best gridded wind product for TC wind analysis.

Before any pre-processing, the HWind analysis provides 1,965 wind snapshots from 157 TCs during 1998–2013. The longitude and latitude of TC centers and the time stamp of the observation platforms are also provided along with the wind information. The symmetric wind profile is obtained by taking the azimuthal average of the HWind wind field relative to the TC center. The maximum wind speed (V_m) and radius of maximum wind (R_m) are then calculated based on the symmetric wind profiles.

Two filters are applied for the HWind analysis: (a) $V_m \geq 18$ m s^{-1} (tropical-storm strength) and (b) $R_m \leq 100$ km. We will analyze the wind field within 5 R_m, and the second filter guarantees that the complete wind information within this range can be extracted from each HWind snapshot. After the filtering, the 1,965 HWind snapshots are reduced to 1,257 wind snapshots, including 643 snapshots of tropical storms ($V_m < 33$ m s^{-1}), 481 of minor tropical cyclones ($V_m \geq 33$ m s^{-1} and <50 m s^{-1}), and 133 of major tropical cyclones ($V_m \geq 50$ m s^{-1}). Since one of the goals in this study is to find the optimal wind model combination to represent the observed TC wind field for storm tide simulation, we confine our wind field analysis within an Earth-relative frame (i.e., the translation effect is not removed from the HWind snapshots).

The HURDAT best-track data (Landsea & Franklin, 2013a, 2013b) is also used to provide the observed minimum central pressure and calculate the local storm translation vector for each HWind snapshot. The local environmental wind shear for each HWind analysis is obtained from the hourly ERA5 reanalysis (Hersbach et al., 2020). The wind shear is defined as the mean wind vector difference between the 200 and 850 hPa and in a circular region out to 5° latitude from the TC center. Before shear is calculated the TC vortex circulation is removed based on the filter algorithm developed by Y. Wang et al., 2015. The basic wind field used to calculate the shear is obtained by iteratively smoothing the zonal and meridional wind fields with a filtering operator. The shear-related results that will be shown are not sensitive to other shear definitions (Y. Wang et al., 2015). The monthly mean ERA5 reanalysis are also employed for general circulation pattern analyses.

21698996, 2022, 17, Downloaded from https://agupubs.onlinelibrary.wiley.com/doi/10.1029/2021JD036359, Wiley Online Library on [20/12/2023]. See the Terms and Conditions (https://onlinelibrary.wiley.com/terms-and-conditions) on Wiley Online Library for rules of use; OA articles are governed by the applicable Creative Commons License

2.2. Wind Models

The CLE15 model will be evaluated with comparison to the H80 model that is used as a model benchmark for the symmetric wind component. The H80 model can be written as:

$$V(r) = \left\{ \left(\frac{R_m}{r} \right)^2 \frac{B\Delta P e^{\left[-\left(\frac{R_m}{r} \right)^B \right]}}{\rho} + \frac{r^2 f^2}{4} \right\}^{1/2} - \frac{fr}{2} \tag{1}$$

where e is the base of natural logarithms, ρ is the air density, f is the Coriolis parameter ($f = 2\Omega \sin \varphi$, where φ is the TC center latitude and $\Omega = 7.292\times 10^{-5}$ s^{-1}), r is the radial distance from TC center, V is the surface wind speed at the radius of r, ΔP is the pressure deficit and calculated as the difference between an environmental pressure of 1,015 hPa for the North Atlantic TCs (Holland, 2008) and the best-track minimum central pressure, and B is the Holland parameter. Following Lin and Chavas (2012), instead of determining B by fitting the model to the whole wind profile, the Holland parameter is calculated by taking V_m at R_m into Equation 1 and yields:

$$B = \frac{V_m^2 e\rho + f V_m R_m e\rho}{\Delta P} \tag{2}$$

Note that Equation 2 only assumes that the reconstructed wind profile can predict a wind speed of V_m at R_m, but the actual predicted maximum wind speed may be occasionally higher than V_m and slightly shifted from R_m. Equations 1 and 2 are based on gradient wind balance that is required for outer-core winds when using the Holland wind model (Hu et al., 2012).

The CLE15 model consists of the inner and outer wind distributions, which can be written as:

$$\left(\frac{M_{inner}}{M_m} \right)^{2-(C_k/C_d)} = \frac{2(r/R_m)^2}{2 - (C_k/C_d) + (C_k/C_d)(r/R_m)^2} \tag{3}$$

$$\frac{\partial M_{outer}}{\partial r} = \chi \frac{(rV)^2}{r_o^2 - r^2} \tag{4}$$

where M_{inner} and M_{outer} are the angular moment in the inner and outer wind regimes, M_m is the angular momentum at R_m, C_k/C_d is the ratio of the exchange coefficients of enthalpy and momentum, χ is given by $2C_d/W_{\text{cool}}$, and r_o is the radius of vanishing wind. The inner and outer wind profiles are connected at a merge point where the angular momentum and its radial derivative are mathematically continuous. Following CLE15, W_{cool} is set to 2×10^{-3} mm s^{-1} and C_k/C_d is estimated as $0.00055V_m^2 - 0.0259V_m + 0.763$ (their Figure 7). The reader is referred to CLE15 for a more detailed procedure for a complete wind profile reconstruction.

Two wind asymmetry approaches are examined, that is, LC12 and CAE20. For the LC12 approach, the TC translation vector is reduced by 40% in magnitude (i.e., a reduction factor of 0.6) and rotated counterclockwise by 20°. The reduction and rotation of translation vector down to the surface can be predicted by the Ekman boundary layer theory, and LC12 quantified the magnitude of reduction and rotation in their statistical analysis. This modified translation vector is then superposed onto each point of the symmetric wind field to generate asymmetry. A more sophisticated procedure is applied using the CAE20 approach which simulates the amplitudes and phases of the asymmetry with eight estimated parameters, TC translation speed and environmental wind shear. The CAE20 model introduces the wind asymmetry by modifying V_m as

$$V_m = \overline{V}_m + A_{tr} \cos[\lambda_{tr} - \phi_{tr}] + A_{sh} \cos[\lambda_{sh} - \phi_{sh}] \tag{5}$$

where

$$A_{tr} = x_{tr.A}^{(0)} + x_{tr.A}^{(1)} V_{tr} \tag{6}$$

$$\phi_{tr} = x_{tr.\phi}^{(0)} + x_{tr.\phi}^{(1)} V_{tr} \tag{7}$$

$$A_{sh} = x_{sh.A}^{(0)} + x_{sh.A}^{(1)} V_{sh} \tag{8}$$

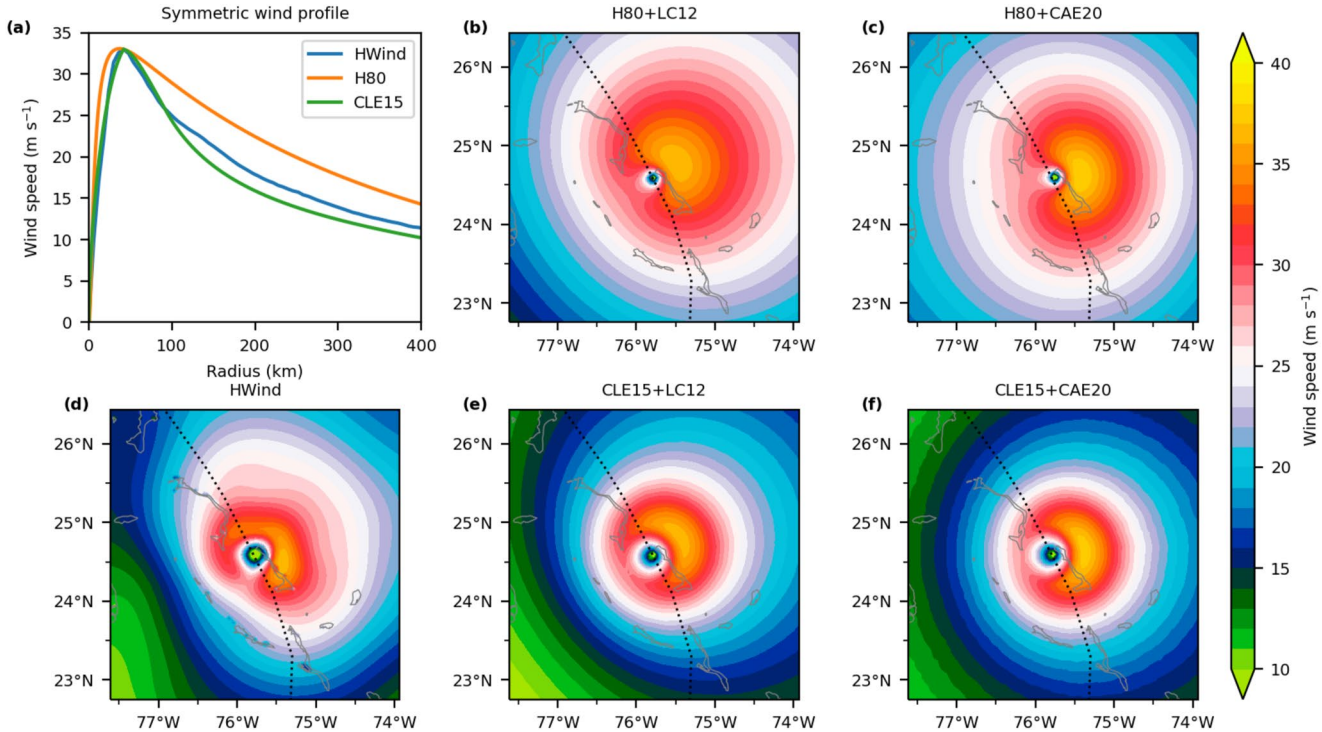

Figure 1. Example of wind field estimation. The plots show the estimated wind field of Hurricane Sandy at 2100 UTC 25 October for (a) the symmetric wind component (i.e., wind profiles) and the full wind fields using the following models: (b) H80 + LC12, (c) H80 + CAE20, (e) CLE15 + LC12 and (f) CLE15 + CAE20. The HWind estimation (d) is shown for comparison. The black dotted line in (b–f) shows the storm track of Hurricane Sandy.

$$\phi_{sh} = x^{(0)}_{sh.b} + x^{(1)}_{sh.b} V_{sh} \tag{9}$$

where $\overline{V}_m$ is the maximum intensity in the symmetric wind field, λ_{tr} and λ_{sh} are the azimuth defined clockwise from the translation and shear directions, and V_{tr} and V_{sh} are the storm translation and shear. The eight empirical parameters are $x^{(0)}_{tr.A}$, $x^{(1)}_{tr.A}$, $x^{(0)}_{tr.b}$, $x^{(1)}_{tr.b}$, $x^{(0)}_{sh.A}$, $x^{(1)}_{sh.A}$, $x^{(0)}_{sh.b}$, and $x^{(1)}_{sh.b}$. Two groups of the eight parameters are given in CAE20, estimated with the Global Forecast System operational analyses (G-group) and Statistical Hurricane Intensity Prediction Scheme database (S-group), respectively. Here we use the "G group" parameters (Table 3 of CAE20) in our analysis, which on average generates the wind field closer to the HWind analysis. In our analysis the full wind field with CAE20 is constructed with the modified V_m (Equation 5) in each azimuth and either H80 or CLE15 symmetric model.

Figure 1 shows an example of symmetric and asymmetric wind estimation of Hurricane Sandy at 21 UTC 25 October 2012 using CLE15, H80, LC12 and CAE20. We can see that for this case H80 overestimates the symmetric wind field inside and outside R_m whereas CLE15 underestimates the wind outside 3 R_m (Figure 1a). The overestimation of wind with H80 remains after coupled with LC12 (Figure 1b) and CAE20 (Figure 1c) compared to the HWind analysis (Figure 1d). The combination of CLE15 + LC12 (Figure 1e) and CLE15 + CAE20 (Figure 1f) can produce similar full wind field as shown by the HWind analysis (Figure 1d).

For comparison, a simple asymmetry wind approach in the Advanced Circulation (ADCIRC) hydrodynamic model is also used but only as another wind forcing option in surge simulations. The asymmetry method in ADCIRC adds in a translation speed weighted by the local symmetric wind speed, with a unity of weight (i.e., a full translation speed) at the radius of maximum wind, and zero weight (i.e., no translational effect) where the local symmetric wind vanishes (Luettich & Westerink, 2018). The simple translation-based approach above, by definition, creates a more pronounced wind asymmetry near the eyewall than in other radial regions.

21698996, 2022, 17, Downloaded from https://agupubs.onlinelibrary.wiley.com/doi/10.1029/2021JD036359, Wiley Online Library on [20/12/2023]. See the Terms and Conditions (https://onlinelibrary.wiley.com/terms-and-conditions) on Wiley Online Library for rules of use; OA articles are governed by the applicable Creative Commons License

21698996, 2022, 17, Downloaded from https://agupubs.onlinelibrary.wiley.com/doi/10.1029/2021JD036359, Wiley Online Library on [20/12/2023]. See the Terms and Conditions (https://onlinelibrary.wiley.com/terms-and-conditions) on Wiley Online Library for rules of use; OA articles are governed by the applicable Creative Commons License

2.3. Storm Tide Observations and Simulations

The impact of different wind field representations on storm tides is investigated by coupling each wind profile with the 2D depth-integrated version of the ADCIRC hydrodynamic model (Luettich et al., 1992). We utilize a high-resolution mesh developed by Marsooli and Lin (2018) that was previously validated against observations of 191 North Atlantic TCs for the period of 1988–2015. In addition to wind forcing, we simulate tides within ADCIRC by incorporating eight tidal constituents obtained from the global model of ocean tides TPXO8-ATLAS (Egbert & Erofeeva, 2002).

The US landfalling TCs for the period of 1988–2020 are selected from the Extended Best Track Database (Demuth et al., 2006). The Extended Best Track Database incorporates all information from the HURDAT database, and additionally includes R_m estimates from 1988 onward. We select TCs with landfall intensity greater than 25.7 m s^{-1} (damaging-force wind) and simulate their storm tides within ADCIRC (132 storms in total). For each historical TC we simulate coastal storm tides using three scenarios: (a) CLE15 symmetric wind plus LC12 asymmetry (CLE15 + LC12), (b) H80 symmetric wind plus LC12 asymmetry (H80 + LC12), and (c) H80 symmetric wind plus the default translational wind asymmetry in ADCIRC (H80 + T) as introduced in Section 2.2. The CAE20 is not used for storm tide simulation as we will show in Section 4 that the LC12 approach can capture the wind asymmetry as well as the CAE20 does but with more simplicity and computational efficiency.

We compare our simulated storm tides against water level observations from 74 tidal gauges maintained by the Center for Operational Oceanographic Products and Services (CO-OPS, www.tidesandcurrents.noaa.gov). For each TC, we select peak water levels from all active tidal gauges within 200 km of the TC track. Tidal gauge measurements are manually inspected, and data is excluded if the gauge stopped recording during a TC passage or if there is clear influence from freshwater discharges on the observed water level. We group the tidal gauges into five regions for discussion: Western Gulf of Mexico (extending until New Orleans, LA), Eastern Gulf of Mexico, Southeast Atlantic (extending until the Chesapeake Bay), Mid-Atlantic (extending until Connecticut), and New England.

2.4. Statistical Significance and Skill Score

A non-parametric bootstrapping is used to examine the statistical significance of the error of simulated winds with different wind models against HWind. The bootstrapping method is applied mainly considering potentially skewed distributions tested here. The two tested distributions are resampled 100,000 times with replacement. The difference of the means between the samples of the two tested distributions is used to form a difference distribution for the means that is used to obtain the statistical significance at 5% level.

To measure the performance of the wind model and storm tide model in reproducing observed peak storm tides, we consider three performance metrics for each coastal region: the mean bias, root mean square error (RMSE), and Wilmott Skill (Willmott, 1981). The Wilmott skill measures the degree of agreement between modeled and observed data, and ranges between 0 (complete disagreement) and 1 (complete agreement). The statistical metrics used here have been widely used in other studies that compare different wind data or surge data (Dullaart et al., 2020; Marsooli et al., 2019; Mayo & Lin, 2019; Torres et al., 2019; Vijayan et al., 2021). We also implement *t*-tests to determine whether differences in modeled storm tide errors across the coastline are statistically significant between different wind models. Specifically, we define storm tide error as the difference between the observed and modeled peak water levels. We utilize a *t*-test to compare the distribution of errors for CLE15 + LC12 compared to H80 + LC12 and H80 + T at the 5% level.

3. Comparison of Symmetric Wind Models

We first compare the CLE15 model outputs with the HWind analysis and use the wind profiles generated by the H80 model as benchmarks. The comparison is conducted in a normalized radial coordinate with respect to R_m. Considering the radial extent of the HWind analysis is 500 km and a large majority of TCs show a R_m of less than 100 km, we examine the model performance within 5 R_m so that any dramatic decrease of sample size at large radii can be avoided when calculating the mean of the normalized profiles. Figure 2a shows that the CLE15 model performs almost perfectly within the merge point (i.e., inner-core region) compared to the mean HWind profile. However, the CLE15 model on average underestimates the wind speed in the outer core, as also shown

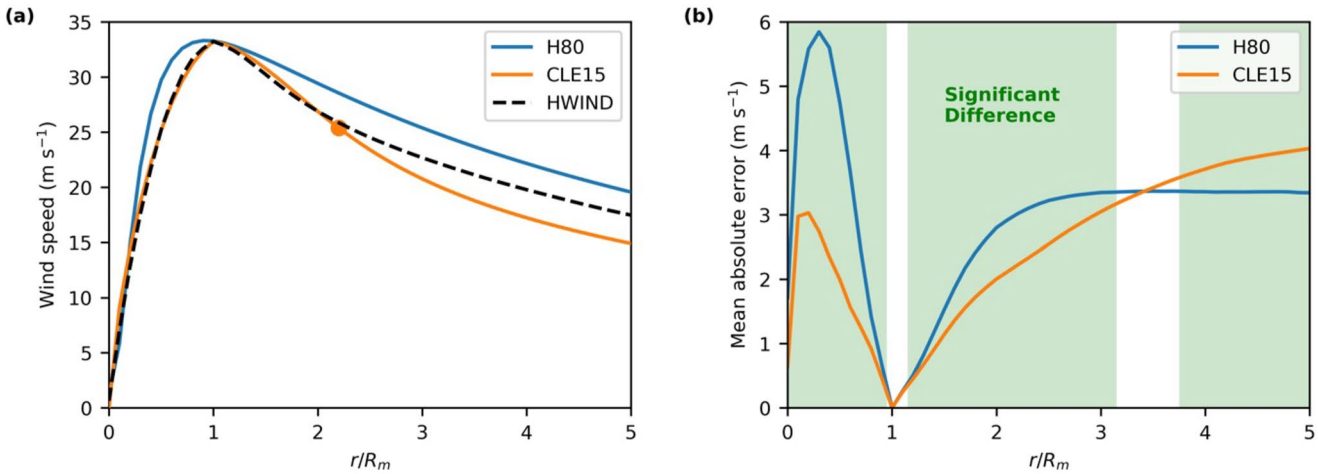

Figure 2. Comparison of the symmetric wind profiles between H80 and CLE15 in a normalized radial coordinate. HWind is used here as reference. (a) Mean wind profiles compared to HWind. The orange dot shows the mean position of the merge point in CLE15. (b) Radial variation of the absolute error (m s^{-1}). The solid lines show the mean of all tropical cyclones (TCs) at different radii. The normalized radial region where the difference is statistically significant between H80 and CLE15 is highlighted with green shadings (Section 2.4).

by Chavas et al. (2015). By the definition of the Holland B parameter calculation in Equation 2, the H80 model can accurately reproduce the V_m at R_m but overestimates the wind speed elsewhere, in line with Holland (1980).

We next calculate the radial profile of the mean absolute errors to examine the superiority of CLE15 and H80 in different radial ranges. Figure 2b shows that the CLE15 model produces a significantly lower error within 3 R_m, whereas the H80 model is superior to CLE15 between 4 and 5 R_m. Figure 3 provides more quantitative details of the performance of H80 and CLE15 by showing the boxplots of absolute errors and biases in 1–3.5 and 3.5–5 R_m, respectively. The median absolute error increases from 1.7 m s^{-1} in 1–3.5 R_m to 2.7 m s^{-1} in 3.5–5 R_m for H80, and from 1.3 m s^{-1} to 3.1 m s^{-1} for CLE15. Consistent with Figure 2a, the median bias of CLE15 is nearly zero in 1–3.5 R_m but changes to −2.3 m s^{-1} in 3.5–5 R_m. H80 shows consistently positive bias in 1–3.5 R_m (1.5 m s^{-1}) and 3.5–5 R_m (2.3 m s^{-1}).

The median and mean of the R_m for the HWind profiles used in this study are 50 and 70 km, respectively. Figures 2 and 3 therefore suggest that within about 200 km from the TC center, the CLE15 model can depict the wind distribution more accurately. Chan and Chan (2015) shows that the global mean radius of gale-force wind is

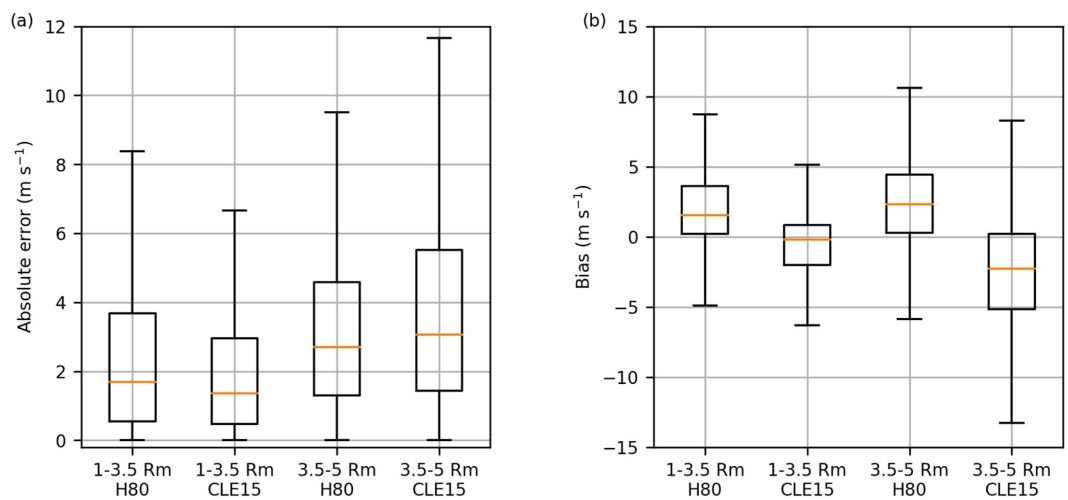

Figure 3. Boxplots for absolute errors and biases within 1–3.5 R_m and 3.5–5 R_m, respectively. Two wind profile models, H80 and CLE15, are compared to the HWind analysis. The orange bar and box show the median and the range from the first to the third quantiles, respectively. The whiskers extend from the box by 1.5 times of the inter-quantile range.

21698996, 2022, 17, Downloaded from https://agupubs.onlinelibrary.wiley.com/doi/10.1029/2021JD036359, Wiley Online Library on [20/12/2023]. See the Terms and Conditions (https://onlinelibrary.wiley.com/terms-and-conditions) on Wiley Online Library for rules of use; OA articles are governed by the applicable Creative Commons License

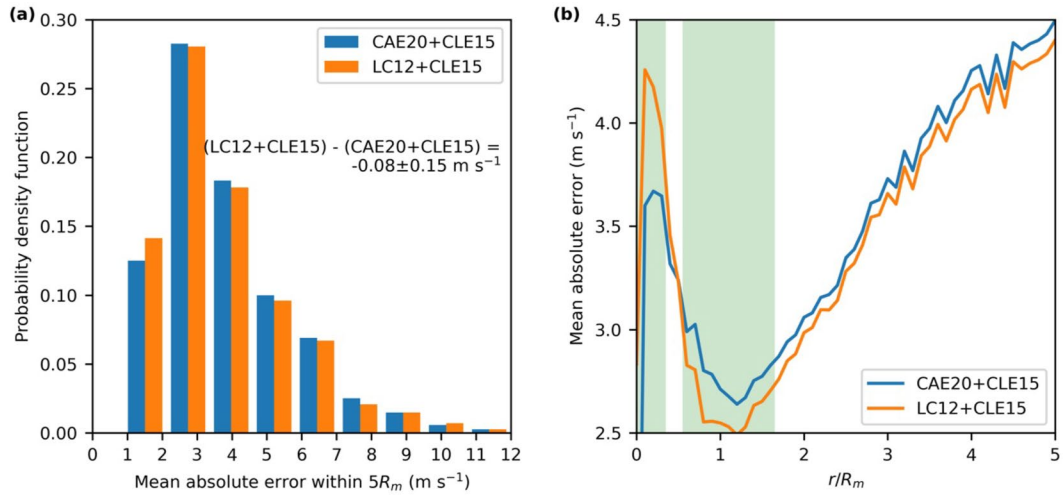

Figure 4. Comparison between the reconstructed wind asymmetry with LC12 and CAE20 against HWind. (a) Mean absolute error (m s^{-1}) within 5 R_m of each tropical cyclone (TC), that is, one error per TC. The mean error difference and 95% confidence intervals are given in the figure. (b) As in Figure 2(c), but for the wind fields reconstructed with LC12 and CAE20.

close to 200 km, which is used to calculate the integrated kinetic energy for TC wind impact estimation (Powell & Reinhold, 2007). As mentioned in the Introduction, storm surge is primarily driven by wind forcing in coastal regions, so the ability to produce an accurate inner-core wind distribution is important to surge simulations. Based on the analysis in Figures 2 and 3, the CLE15 model can provide a better representation of the observed winds than H80 for the crucial inner-core region where the high winds exist.

4. Comparison of Asymmetric Wind Models

We next examine two asymmetric wind approaches, that is, LC12 and CAE20, coupled with the CLE15 model. Figure 4a shows that for the case-averaged error, the performance of the two approaches does not show a significant difference within 5 R_m, although the LC12 approach produces a lower mean absolute error, which can also be seen in Figure 4b from 0.5 R_m outwards. The LC12 approach appears to generate a significant larger error within 0.5 R_m (Figure 4b), which is due to a horizontally uniform superposition of the surface background wind. As shown in LC12 (their Figure 2), the background wind within the eyewall reduces rapidly relative to the TC motion speed when approaching the center of the eye, which indicates that the large error within 0.5 R_m can be corrected with a parametric reduction factor as a function of radius. However, following LC12, we keep a fixed reduction factor in the following analysis for simplicity as the effect of such a correction in the low wind region is negligible on storm tide simulations (not shown). For the critical region around R_m where the extreme winds are located, the lower error with the LC12 approach becomes significant compared to using the CAE20 model (Figure 4b).

As mentioned in the Introduction, the wind asymmetry is mainly related to the TC motion and wind shear. It is therefore important to examine if the asymmetric models can reproduce the locations of the maximum wind relative to the directions of motion and shear, respectively. With the HWind analysis, we observe a mean V_m location to the right of the TC motion direction (Figure 5a). The observed location of V_m also shows a slight rotation to the up-motion-right quadrant. Both LC12 (Figure 5b) and CAE20 (Figure 5c) approaches can correctly reproduce the V_m location to the right of motion direction. Due to the 20° counterclockwise rotation of the translation vector, the mean V_m location with the LC12 approach, however, shows a weak rotation to the down-motion-right quadrant, which is different from the mean location in HWind and using the CAE20 approach, but consistent with theoretical predictions in an earth-relative frame (Shapiro, 1983; Thomsen et al., 2015).

If the HWind snapshots are aligned with the vertical shear direction, the V_m is located to the left along the shear direction (Figure 5d), in line with the observational studies by Klotz and Jiang (2016, their Figure 3a) in an earth-relative frame. If the translation effect is removed (i.e., in a storm-relative frame), previous studies showed that the maximum wind speed is also located to the left of the shear direction (Klotz & Jiang, 2017; Ueno &

21698996, 2022, 17, Downloaded from https://agupubs.onlinelibrary.wiley.com/doi/10.1029/2021JD036359, Wiley Online Library on [20/12/2023]. See the Terms and Conditions (https://onlinelibrary.wiley.com/terms-and-conditions) on Wiley Online Library for rules of use; OA articles are governed by the applicable Creative Commons License

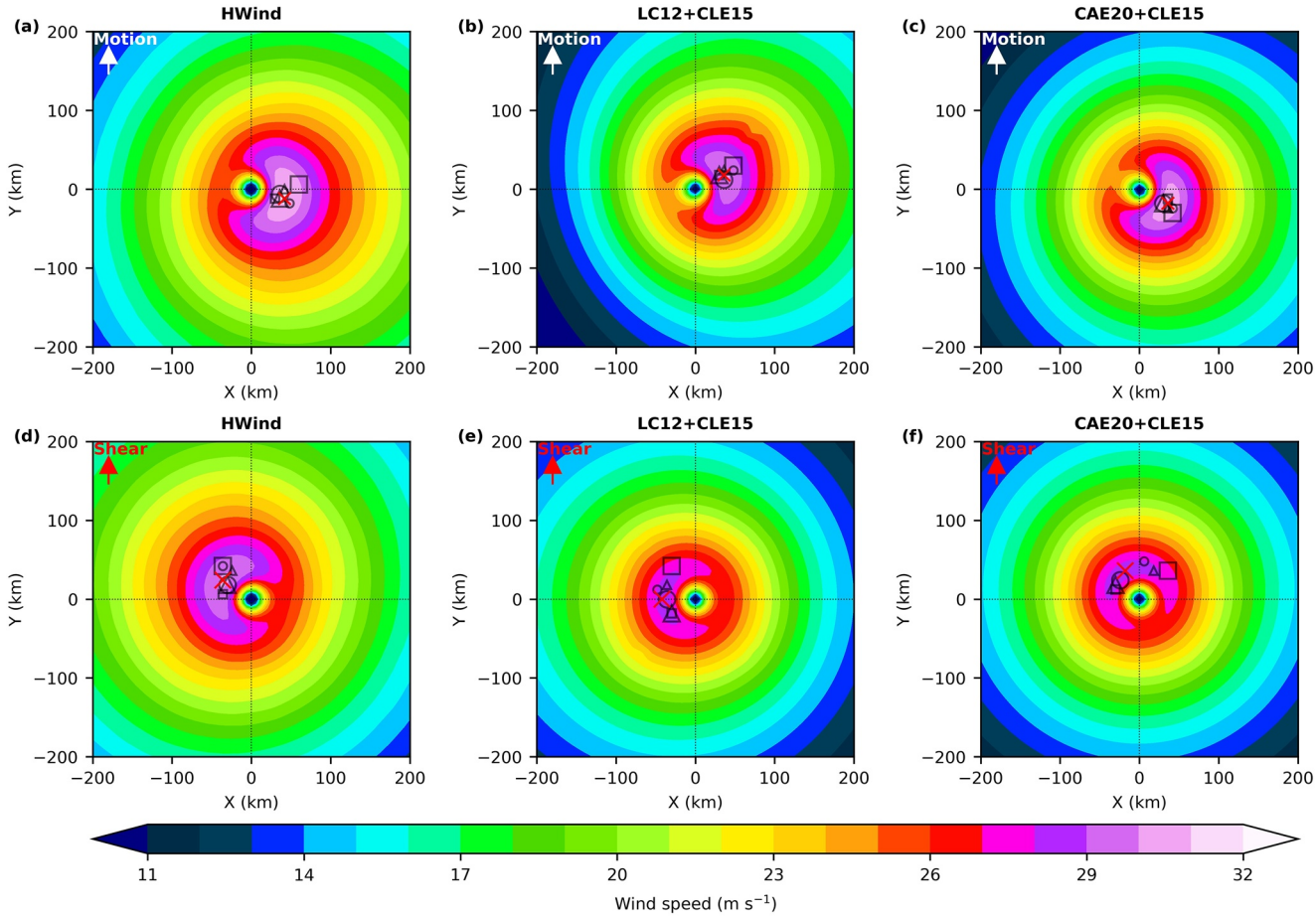

Figure 5. Wind field composite for (a and d) HWind (b and e) LC12 + CLE15 approach, and (c and f) CAE20 + CLE15 approach. The wind fields are aligned with (a–c) tropical cyclones motion direction, and (d–f) vertical wind shear direction, respectively. The red "×" shows the mean location of maximum wind speed by compositing all the samples. The locations of maximum wind are shown with circles for intensity subsets, triangles for translation speed subsets, and squares for shear subsets. The medians of intensity (32 m s^{-1}), translation (4.8 m s^{-1}) and shear (8.1 m s^{-1}) are used to separate subsets, that is, three pairs of subsets for intensity, translation and shear are analysis. In each pair of subsets, the larger (smaller) marker represents the subset with the values above (below) the median.

Bessho, 2011; Uhlhorn et al., 2014). This rotation of V_m location relative to shear direction can also be reproduced by the LC12 (Figure 5e) and CAE20 (Figure 5f) approaches, however, with a slight counterclockwise rotation for the former, and clockwise for the latter.

Figure 5 also shows the mean locations of maximum wind speed by breaking down the whole sample into three paired subsets according to the medians of intensity (> and <32 m s^{-1}), translation speed (> and <4.8 m s^{-1}) and shear (> and <8.1 m s^{-1}), respectively. When the composite is aligned with the motion direction, the locations of maximum wind in each pair of subsets does not show much variation from the location with all samples (Figures 5a–5c), apart from the samples under high wind shear (marked with larger squares) showing a longer distance between the maximum wind location and TC center. If the composite is aligned with the shear direction, the locations of maximum wind in the subsets of reconstructed wind fields (Figures 5e and 5f) show a larger variability compared to that with HWind (Figure 5d). The variability by using LC12 (Figure 5e) and CAE20 (Figure 5f) are comparable.

Shear information is required as an input by the CAE20 approach, but it is surprising that the LC12 approach can also correctly reproduce the V_m location to the left of shear direction, in which no shear information is directly used for wind asymmetry at all. It should be noted that Figure 5 may not reveal the detailed impact related to motion and shear on the wind asymmetry since the translation effect is not removed from the field (i.e., not in a storm-relative frame). Nevertheless, Figure 5 indicates a general correlation between the TC motion direction and vertical wind shear direction in an earth-relative frame, which will be explored next.

21698996, 2022, 17, Downloaded from https://agupubs.onlinelibrary.wiley.com/doi/10.1029/2021JD036359, Wiley Online Library on [20/12/2023]. See the Terms and Conditions (https://onlinelibrary.wiley.com/terms-and-conditions) on Wiley Online Library for rules of use; OA articles are governed by the applicable Creative Commons License

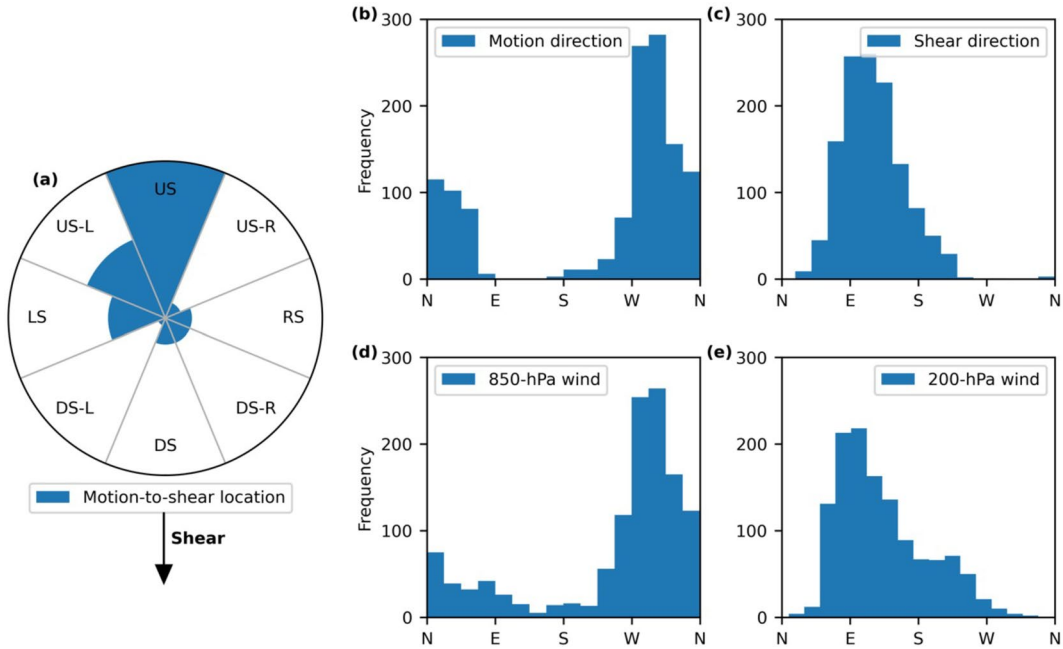

Figure 6. Relationship between tropical cyclone (TC) motion and vertical wind shear directions. (a) Relative frequency of TC motion directions with respect to shear directions. A pie is divided into 8 wedges: upshear (US), upshear right (US-R), right of shear (RS), downshear right (DS-R), downshear (DS), downshear left (DS-L), left of shear (LS) and upshear left (US-L). The shear direction of all TCs is aligned as shown by the black arrow. (b) TC motion direction. (c) Shear direction. (d) Wind direction at 850 hPa. (e) Wind direction at 200 hPa. The geographical orientations (e.g., N, E, S and W) shows the directions which wind vectors or motions point to.

Figure 6a shows that for the North Atlantic storms the TC-related local vertical wind shear most frequently appears in the opposite direction of TC motion. The motion direction generally points to the northwest in the selected cases of this study (Figure 6b), whereas the local shear direction is toward the east (Figure 6c). By

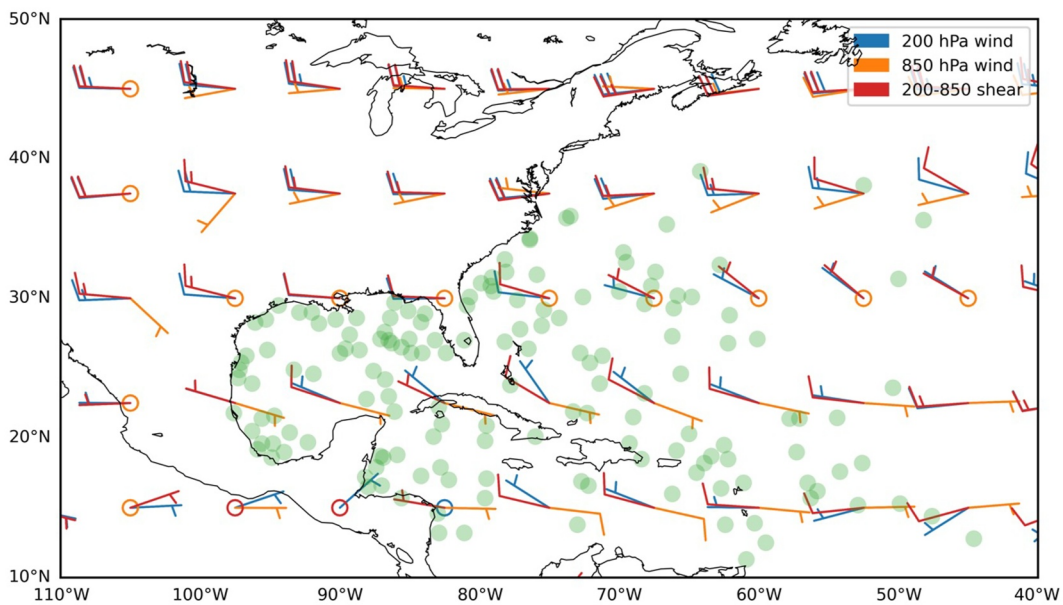

Figure 7. Mean upper (200 hPa) and lower (850 hPa) wind bars and vertical wind shear between the two calculated from the ERA5 monthly reanalysis from August to October (the North Atlantic hurricane season) for 1980–2020. The green dots show the location where HWind analysis is used.

21698996, 2022, 17, Downloaded from https://agupubs.onlinelibrary.wiley.com/doi/10.1029/2021JD036359, Wiley Online Library on [20/12/2023]. See the Terms and Conditions (https://onlinelibrary.wiley.com/terms-and-conditions) on Wiley Online Library for rules of use; OA articles are governed by the applicable Creative Commons License

21698996, 2022, 17, Downloaded from https://agupubs.onlinelibrary.wiley.com/doi/10.1029/2021JD036359, Wiley Online Library on [20/12/2023]. See the Terms and Conditions (https://onlinelibrary.wiley.com/terms-and-conditions) on Wiley Online Library for rules of use; OA articles are governed by the applicable Creative Commons License

breaking down the shear into 850- and 200 hPa winds, it is found that the 850 hPa wind shares a very similar distribution to the motion direction, which can be explained by a similar distribution of wind direction at the steering level (600 hPa, not shown). The wind direction aloft (at 200 hPa, Figure 6e) points generally to the east, which is controlled by the westerlies.

Further analysis reveals that the connection between TC motion and local shear directions of individual TCs in the North Atlantic can be partly understood with the general circulation pattern. Figure 7 shows the mean 200- and 850 hPa winds and the wind shear between the two during the main hurricane season (August–October). The domain-averaged standard deviation of each grid point in Figure 7 is 4.1 m s^{-1} for the shear speed, and 35° for the shear direction. Based on the spatial change of upper and lower winds, the latitudinal band around 30°N divides the shear-related circulation into three regimes. To the South of 30°N, the 850 hPa wind is dominated by the trade wind, the 200 hPa wind is partly controlled by the upper-level westerlies, and the wind directions at 850 and 200 hPa are therefore opposed. Based on the shear definition of wind vector difference, the vertical wind shear in the southern regime points to the east. Around 30°N, the 850 hPa wind is weak whereas the 200 hPa westerlies maintains. The shear direction in the middle regime therefore shares the same direction of 200 hPa wind and, again, points to the east. To the North of 30°N, both wind directions at 200 and 850 hPa are dominated by the westerlies. Due to an increase of wind speed with height in the northern regime, the shear direction is still toward the east. In our analysis most of the cases are in the two regimes at lower latitudes.

Figures 6 and 7 show that the general TC motion and local shear directions in our analysis are opposed. It should be noted that the monthly mean analysis in Figure 7 can only partially explain the results in Figure 6, which is based on instantaneous wind shear. Nevertheless, Figures 6 and 7 indicate a strong preference for storms to move counter to the shear direction. As a result, there is a right-to-left flip of the maximum wind location when the orientation of the coordinate system is changed between motion and shear directions in Figure 5. The statistically opposed directions of motion and shear explain why the LC12 approach can generate the correct location of maximum wind even without explicitly accounting for the shear effect. The angle between TC motion and shear directions were previously analyzed but the conclusions are diverse (Corbosiero & Molinari, 2003; Franklin et al., 1993; Marks et al., 1992), which could be limited by the small number of observations. Based on an analysis of 35 TCs in 128 flight observations, Uhlhorn et al. (2014) found a prevailing shear pointing to the east with a general TC motion to the west, which supports the opposed directions of shear and TC motion as shown in our analysis. Considering the model simplicity, wind representation accuracy and computational efficiency, our analysis suggests that the LC12 approach is superior to CAE20 as a wind asymmetry model. Thus, in the following surge simulations we only apply the LC12 approach coupled with symmetric models to generate wind forcings.

5. Storm Tidal Simulations

We examine differences in modeled TC-induced storm tides forced by different wind field representations, that is, CLE15 + LC12, H80 + LC12, and H80 + T winds. The H80 + T, that is, the H80 symmetric wind plus the default translational wind asymmetry in ADCIRC, is used here as a reference method since it is the default wind forcing combination in ADCIRC for storm surge simulations. For each wind field scenario, we compare modeled peak storm tides against peak water levels from tidal gauge observations. By calculating the modeled storm tide bias across the whole US eastern coastline, we find that the CLE15 + LC12 model yields the lowest mean bias (−0.07 m) compared to both H80 + LC12 (−0.12 m) and H80 + T (−0.13 m). The CLE15 + LC12 mean bias is significantly lower than the H80 + LC12 bias (p-value = 0.001) and the H80 + T bias (p-value < 0.001), based on the results from a two-sample t-test.

Table 1 reports the performance metrics in five regions of the US eastern coastline. Overall, the CLE15 + LC12 wind scenario performs the best since it produces the highest skill score and lowest bias for each region. Along the Southeast and Middle Atlantic coast the CLE15 + LC12 scenario produces slightly higher RMSE than H80 + LC12, but still has lower RMSE than H80 + T. In general, the H80 + LC12 scenario yields similar skill as CLE15 + LC12 along the Southeast and Middle Atlantic coast but performs worse than CLE15 + LC12 along the Gulf of Mexico. In contrast, H80 + T performs worse than the other two scenarios for all regions of the coastline, except the western Gulf of Mexico where H80 + T and CLE15 + LC12 perform similarly well.

In the Gulf of Mexico, due to the shape of the coastline, wide continental shelf, and small tidal constituents, storm tides are sensitive to the full wind profile, rather than just the maximum wind speed at landfall (Irish et al., 2008; Resio & Westerink, 2008). Figure 8 confirms that switching from the H80 symmetrical wind model to CLE15

21698996, 2022, 17, Downloaded from https://agupubs.onlinelibrary.wiley.com/doi/10.1029/2021JD036359, Wiley Online Library on [20/12/2023]. See the Terms and Conditions (https://onlinelibrary.wiley.com/terms-and-conditions) on Wiley Online Library for rules of use; OA articles are governed by the applicable Creative Commons License

Table 1
Comparison of Modeled Peak Storm Tide Performance Metrics for Each Wind Field Scenario and Each Coastline Region

	CLE15 + LC12			H80 + LC12			H80 + T		
Region	RMSE	Bias	Skill	RMSE	Bias	Skill	RMSE	Bias	Skill
W. GoM	0.40	**0.00**	**0.92**	0.41	−0.11	0.90	**0.39**	−0.10	**0.92**
E. GoM	**0.46**	**−0.08**	**0.85**	0.48	−0.19	0.80	0.51	−0.21	0.76
SE. Atl.	0.24	**−0.06**	**0.90**	**0.22**	−0.09	**0.90**	0.28	−0.08	0.86
M. Atl.	0.28	**−0.09**	**0.91**	**0.26**	−0.15	**0.91**	0.32	−0.18	0.87
N.E.	**0.14**	**0.01**	**0.98**	**0.14**	**0.01**	**0.98**	0.20	−0.02	0.96

Note. "RMSE" refers to the root-mean-square-error of modeled storm tides, "Bias" refers to the mean difference between modeled and observed peak water level (where negative values indicate model under-prediction), and "Skill" refers to the Willmott Skill (ranging from 0 to 1). W. GoM: Western Gulf of Mexico (extending until New Orleans, LA); E. GoM: Eastern Gulf of Mexico; SE. Atl.: Southeast Atlantic (extending until the Chesapeake Bay); M. Atl.: Mid-Atlantic (extending until Connecticut); N.E.: New England. Numbers in bold signify the best performance values for each coastal region.

brings the largest improvement to surge simulation in this region. Along the western Gulf of Mexico (Figures 8a and 8b) both CLE15 + LC12 and H80 + LC12 perform well for low surge events, but CLE15 + LC12 is considerably superior for extremely high surge events. H80 + T performs with higher skill compared to H80 + LC12 in the western Gulf of Mexico, especially for high surge events. This is likely because the addition of the full

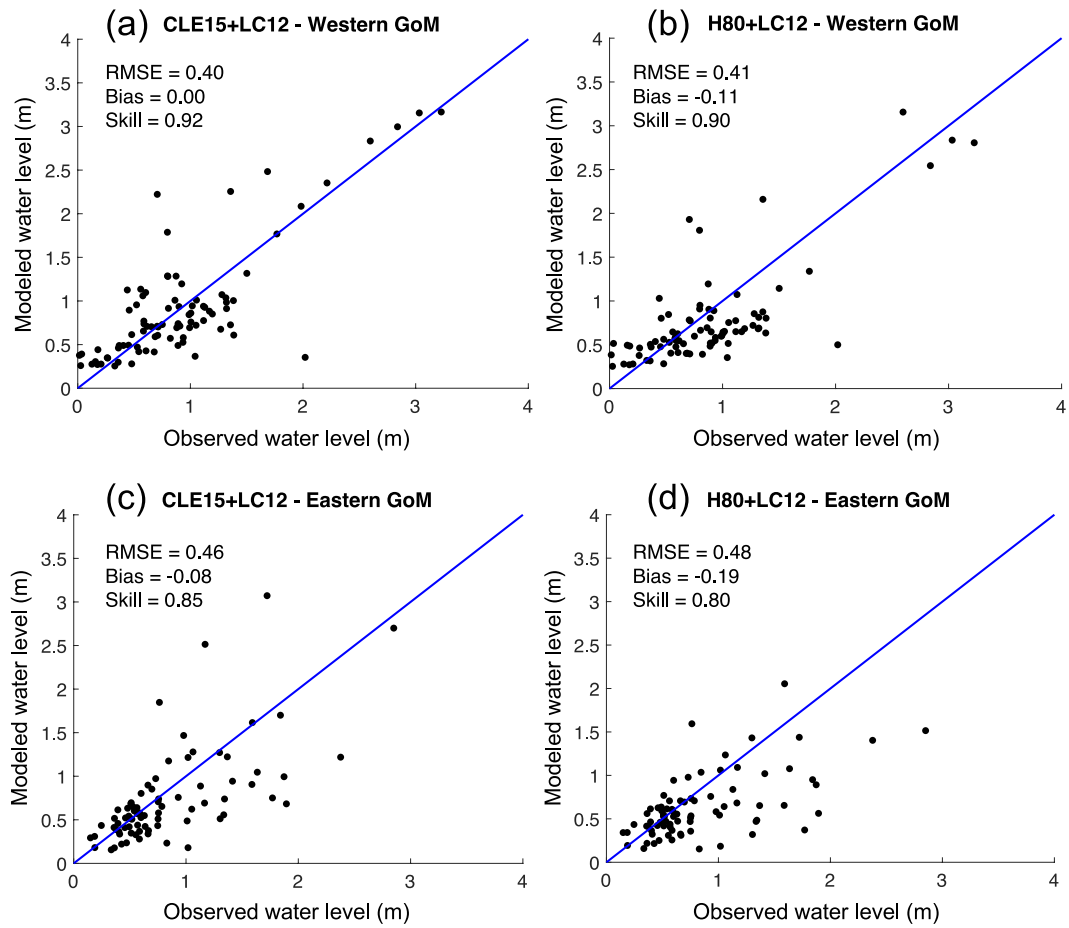

Figure 8. Comparison of observed and modeled peak storm tides (m) using the CLE15 + LC12 wind (a and c) and the H80 + LC12 wind (b and d) for the (a and b) western and (c and d) eastern Gulf of Mexico. The thin blue line represents the $y = x$ line.

translation speed vector at the radius of maximum winds makes up for the lower azimuthal wind speed predicted by H80, yielding higher overall storm tide estimates. Along the eastern Gulf of Mexico (Figures 8c and 8d) H80 + LC12 approach systematically underestimates moderate-extreme surge events that are better simulated with the CLE15 + LC12 winds.

Although the mean wind profile for the H80 model has higher values than the CLE15 model for both the inner and outer winds (Figure 2a), the H80 wind model tends to underestimate the wind field for high intensity TCs compared to other wind models (Lin & Chavas, 2012). Thus, for high intensity TCs the H80 model may underestimate peak storm tides when coupled with ADCIRC. To illustrate this point, Figure 9 shows modeled and observed wind fields and storm tides for Hurricane Gustav (2008), which made landfall in Louisiana as a Category 2 storm.

Figures 9a and 9b show a comparison between modeled and observed peak storm tides at all tidal gauges (depicted in each figure as circles colored by the water level difference between modeled and observed storm tide) within 200 km of Gustav's track using the CLE15 + LC12 and H80 + LC12 models, respectively. Blue markers indicate model underprediction of peak water level and red indicates model overprediction. Both models can reproduce peak storm tides on the left-hand side (LHS) of the storm, where storm surges were small. However, on the right-hand side (RHS), H80 + LC12 significantly underestimates the peak storm tide at the Shell Beach water level gauge (Figure 9c). The H80 + T model underestimates even further the peak storm tides from Gustav on the RHS along the storm track (Figure 9c). Examining the time history of Gustav's wind at Shell Beach (marked with a red circle in Figure 9a) reveals that the H80 profile results in lower total wind speeds compared to the CLE15 profile pre landfall (Figure 9d). In addition, the H80 models underestimate the westward component of the wind compared to CLE15 + LC12 (Figure 9e), resulting in less storm surge reaching the Shell Beach. The reason for the CLE15 model to generate a stronger local westward wind at Shell Beach is because the wind model produces higher wind speeds in the outer region compared to H80 in this case. Additionally, the application of the LC12 background wind, which applies a counterclockwise rotation of the TC translation vector, also increases the westward wind speed (Figure 9e) and reduces the northward wind (Figure 9f) locally at Shell Beach compared to that with H80 + T.

Storm tides can also be sensitive to storm motion speed when a TC moves relatively fast (Thomas et al., 2019), in which case the choice of asymmetric wind model becomes even more important. The background wind of these fast-moving storms may make up a larger portion of the total TC wind compared to slow-moving ones. By comparing the H80 + LC12 and H80 + T performance metrics (Table 1), for the Southeast and Middle Atlantic and New England, where the mean TC motion speed at landfall (11 m s^{-1}) is 10% faster than that in the Gulf of Mexico (10 m s^{-1}), we see that incorporating the LC12 wind asymmetry results in an improvement in the storm tide simulation results.

In Figure 10 we show the example of Hurricane Bob (1991), which made landfall in Rhode Island as a Category 2 storm. In our analysis Bob is the fastest-moving TC at landfall, with a translation speed of 20 m s^{-1}, 90% faster than the mean translation speed at landfall of all the storms simulated here. The comparison of modeled and observed peak storm tides for Bob reveals that both CLE15 + LC12 and H80 + LC12 perform well (Figures 10a and 10c), but H80 + T overestimates the peak storm tide at gauges on both the LHS and RHS of the storm track (Figure 10b). In this case the H80 + T combination greatly overestimates the storm surge at gauges close to the TC track, demonstrated by the comparison of water level time series at Providence, RI (Figure 10c). The large overestimation in storm tides is due to the application of the full translation speed vector to the symmetric wind field around R_m where the high winds are crucial for peak surges, and the lack of a counterclockwise rotation of the translation effect as in LC12. Figures 10e and 10f show that the westward and northward components of wind are similar between CLE15 + LC12 and H80 + LC12, but different for H80 + T. Since the translation vector of Bob points northward, H80 + T adds more velocity to the meridional direction compared to H80 + LC12 (where the translation vector is rotated 20° counterclockwise; Figure 10f), and H80 + T has a weaker zonal-wind asymmetry of the wind field compared to CLE15 + LC12 and H80 + LC12 (Figure 10e). Because the total translation speed of Bob is relatively large and since large forward speed is associated with higher peak storm surges (Thomas et al., 2019), the impact of the asymmetry method significantly alters the peak storm tides.

21698996, 2022, 17, Downloaded from https://agupubs.onlinelibrary.wiley.com/doi/10.1029/2021JD036359, Wiley Online Library on [20/12/2023]. See the Terms and Conditions (https://onlinelibrary.wiley.com/terms-and-conditions) on Wiley Online Library for rules of use; OA articles are governed by the applicable Creative Commons License

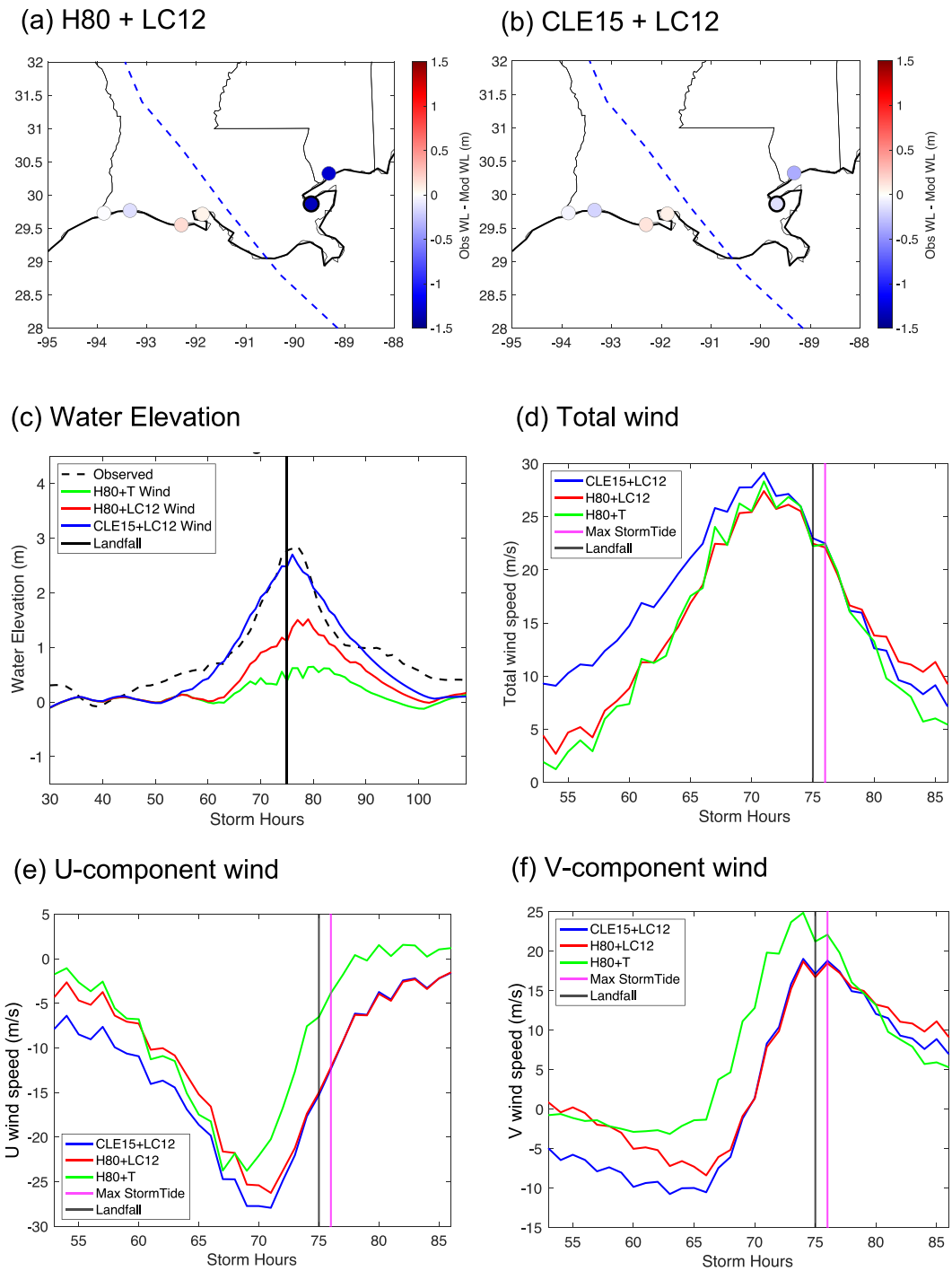

Figure 9. Comparison of observed (Obs) and modeled (Mod) peak water level (WL) during Hurricane Gustav (2008) at tidal gauges within 200 km of storm center, where each tidal gauge is depicted as a circular marker, using (a) H80 + LC12 wind and (b) CLE15 + LC12 wind. The color of each tidal gauge marker corresponds to the water level difference between the observation and model, where blue indicates model underprediction and red indicates model overprediction. Blue dashed line represents Gustav's track. (c) Observed and modeled water level time series during Hurricane Gustav (2008) at Shell Beach, LA tidal gauge (# 8761305), where the location of the Shell Beach tidal gauge is shown in (a) and (b) as a black circle, using CLE15 + LC12 wind (blue), H80 + LC12 wind (red) and H80 + T wind (green). Time series of wind speed at Shell Beach, LA for (d) total wind speed, (e) U-direction component of wind (where negative values indicate westward velocity), and (f) V-direction component of wind (where positive values indicate northward velocity). The reference time in (c–f) is 1400 UTC 29 August 2008.

21698996, 2022, 17, Downloaded from https://agupubs.onlinelibrary.wiley.com/doi/10.1029/2021JD036359, Wiley Online Library on [20/12/2023]. See the Terms and Conditions (https://onlinelibrary.wiley.com/terms-and-conditions) on Wiley Online Library for rules of use; OA articles are governed by the applicable Creative Commons License

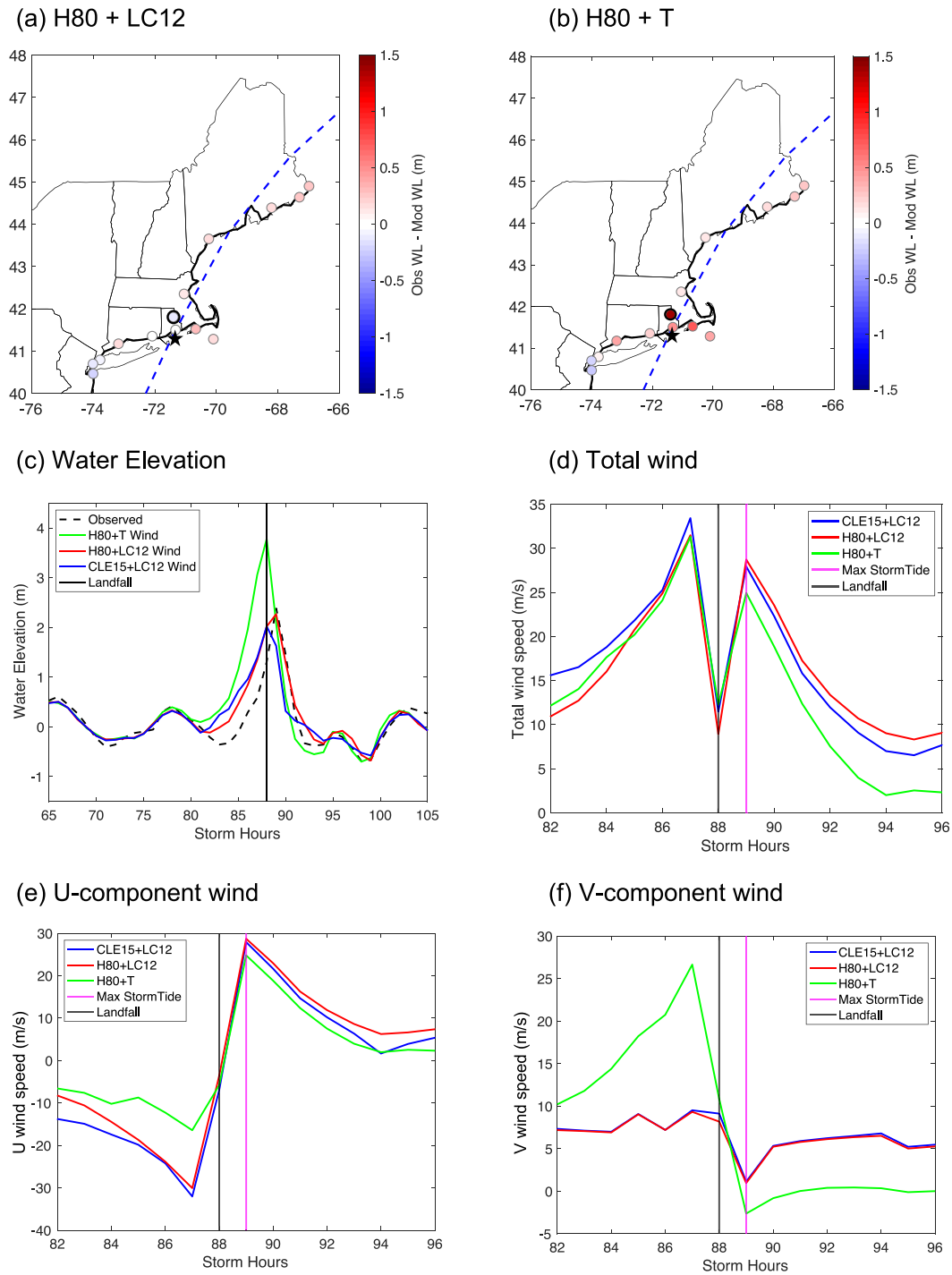

Figure 10. Comparison of observed (Obs) and modeled (Mod) peak water level (WL) during Hurricane Bob (1991) at tidal gauges within 200 km of storm center using (a) H80 + LC12 wind and (b) H80 + T wind. The color of each tidal gauge marker corresponds to the water level difference between the observation and model, where blue indicates model underprediction and red indicates model overprediction. Blue dashed line represents Bob's track. (c) Observed and modeled water level time series during Hurricane Bob (1991) at Providence, RI tidal gauge (# 8454000), where the location of the Providence tidal gauge is shown in (a) and (b) as a black circle, using CLE15 + LC12 wind (blue), H80 + LC12 wind (red) and H80 + T wind (green). Time series of wind speed at Narragansett Bay opening (marked by the black star in a and b) for (d) total wind speed, (e) U component of wind (zonal), and (f) V component of wind (meridional). The reference time in (c–(f) is 0200 UTC 16 August 1991.

21698996, 2022, 17, Downloaded from https://agupubs.onlinelibrary.wiley.com/doi/10.1029/2021JD036359, Wiley Online Library on [20/12/2023]. See the Terms and Conditions (https://onlinelibrary.wiley.com/terms-and-conditions) on Wiley Online Library for rules of use; OA articles are governed by the applicable Creative Commons License

21698996, 2022, 17, Downloaded from https://agupubs.onlinelibrary.wiley.com/doi/10.1029/2021JD036359, Wiley Online Library on [20/12/2023]. See the Terms and Conditions (https://onlinelibrary.wiley.com/terms-and-conditions) on Wiley Online Library for rules of use; OA articles are governed by the applicable Creative Commons License

6. Summary

The TC-related major hazards are all closely related to the surface wind field that can be broken down into symmetric and asymmetric components. Several models have been developed to represent the wind conditions for these two components. For the symmetric wind, we evaluate a physics-based complete wind profile model (CLE15) against HWind with the widely used Holland model (H80) as a benchmark model for comparison. We find that the CLE15 model performs significantly better than the H80 within 3 R_m. This is the TC radial range covering about the areas with at least gale-force wind where most damage happens. For the asymmetric wind component, we find that the LC12 approach performs as well as a recently developed wind asymmetry model (CAE20), but with more simplicity and higher computational efficiency. The LC12 approach implicitly accounts for the vertical wind shear impact on wind asymmetry via the climatological linkage between shear and TC motion directions. It should be noted that the climatological linkage mentioned above should not be expected in every individual TCs due to the large variability of synoptic scenarios from case to case. Nevertheless, our results show that from a statistical perspective, LC12 can provide a reasonable asymmetric wind field as a storm tide forcing.

Storm tide simulations of the U.S. landfalling TCs confirm that the integration of CLE15 and LC12 produces the highest skill score among all the wind model combinations examined in both the Gulf of Mexico and the U.S. Atlantic coast. The main improvement in the Gulf of Mexico is brought by the application of CLE15 for the symmetric wind field. The advantage of using the LC12 asymmetric approach becomes clear for fast-moving storms compared to the translation-speed-based approach in ADCIRC as a default option. Based on the analysis of this study, we suggest that the physics-based wind profile model (CLE15) coupling with the surface-background-wind approach (LC12) is a superior way of simulating TC-induced storm tides in lieu of the Holland model with translation-speed-based asymmetric approach in the North Atlantic, and perhaps, elsewhere. The CLE15 + LC12 approach has been incorporated into the ADCIRC model framework.

Data Availability Statement

The CLE15 + LC12 wind model and a description of its integration with the ADCIRC framework are deposited to the NSF DesignSafe-CI and can be accessed online (https://doi.org/10.17603/ds2-xd0r-bk81) [Software]. The HWind analysis used in this study is publicly assessable via its Legacy Archive page (registration required): https://www.rms.com/event-response/hwind/legacy-archive/ [Dataset]. The tropical cyclone best track data used in this study can be downloaded from the National Hurricane Center website (https://www.nhc.noaa.gov/data/%23hurdat) [Dataset]. The ERA5 reanalysis data is available at the European Centre for Medium-Range Weather Forecasts (https://cds.climate.copernicus.eu/cdsapp%23%21/dataset/reanalysis%2Dera5%2Dpressure%2Dlevels%3Ftab%3Dform) [Dataset].

Acknowledgments
We thank three anonymous reviewers for helping improve the manuscript. This study is supported by National Science Foundation (Grant 1652448) and Princeton Intellectual Property Accelerator Fund program.

References

Anthes, R. A. (1982). *Tropical cyclones-Their evolution, structure and effects*. The American Meteorological Society.

Bernardet, L., Tallapragada, V., Bao, S., Trahan, S., Kwon, Y., Liu, Q., et al. (2015). Community support and transition of research to operations for the hurricane weather research and forecasting model. *Bulletin of the American Meteorological Society*, *96*(6), 953–960. https://doi.org/10.1175/bams-d-13-00093.1

Chan, K. T. F., & Chan, J. C. L. (2015). Global climatology of tropical cyclone size as inferred from QuikSCAT data. *International Journal of Climatology*, *35*(15), 4843–4848. https://doi.org/10.1002/joc.4307

Chang, D., Amin, S., & Emanuel, K. (2020). Modeling and parameter estimation of hurricane wind fields with asymmetry. *Journal of Applied Meteorology and Climatology*, *59*(4), 687–705. https://doi.org/10.1175/jamc-d-19-0126.1

Chavas, D. R., & Lin, N. (2016). A model for the complete radial structure of the tropical cyclone wind field. Part II: Wind field variability. *Journal of the Atmospheric Sciences*, *73*(8), 3093–3113. https://doi.org/10.1175/jas-d-15-0185.1

Chavas, D. R., Lin, N., & Emanuel, K. (2015). A model for the complete radial structure of the tropical cyclone wind field. Part I: Comparison with observed structure. *Journal of the Atmospheric Sciences*, *72*(9), 3647–3662. https://doi.org/10.1175/jas-d-15-0014.1

Corbosiero, K. L., & Molinari, J. (2003). The relationship between storm motion, vertical wind shear, and convective asymmetries in tropical cyclones. *Journal of the Atmospheric Sciences*, *60*(2), 366–376. https://doi.org/10.1175/1520-0469(2003)060<0366:trbsmv>2.0.co;2

Demuth, J. L., DeMaria, M., & Knaff, J. A. (2006). Improvement of advanced microwave sounding unit tropical cyclone intensity and size estimation algorithms. *Journal of Applied Meteorology and Climatology*, *45*(11), 1573–1581. https://doi.org/10.1175/jam2429.1

Depperman, C. E. (1947). Notes on the origin and structure of philippine typhoons. *Bulletin America Meteorology Social*, *28*(9), 399–404. https://doi.org/10.1175/1520-0477-28.9.399

Dinapoli, S. M., Bourassa, M. A., & Powell, M. D. (2012). Uncertainty and intercalibration analysis of H*Wind. *Journal of Atmospheric and Oceanic Technology*, *29*(6), 822–833. https://doi.org/10.1175/jtech-d-11-00165.1

Dullaart, J. C. M., Muis, S., Bloemendaal, N., & Aerts, J. C. J. H. (2020). Advancing global storm surge modelling using the new ERA5 climate reanalysis. *Climate Dynamics*, *54*(1–2), 1007–1021. https://doi.org/10.1007/s00382-019-05044-0

Egbert, G. D., & Erofeeva, S. Y. (2002). Efficient inverse modeling of Barotropic Ocean tides. *Journal of Atmospheric and Oceanic Technology*, *19*(2), 183–204. https://doi.org/10.1175/1520-0426(2002)019<0183:eimobo>2.0.co;2

Emanuel, K. (2004). Tropical cyclone energetics and structure. In *Atmospheric turbulence and Mesoscale meteorology* (pp. 165–192). Cambridge University Press.

Emanuel, K. (2017a). A fast intensity simulator for tropical cyclone risk analysis. *Natural Hazards*, *88*(2), 779–796. https://doi.org/10.1007/s11069-017-2890-7

Emanuel, K. (2017b). Assessing the present and future probability of Hurricane Harvey's rainfall. *Proceedings of the National Academy of Sciences of the United States of America*, *114*(48), 12681–12684. https://doi.org/10.1073/pnas.1716222114

Emanuel, K., & Rotunno, R. (2011). Self-stratification of tropical cyclone outflow. Part I: Implications for storm structure. *Journal of the Atmospheric Sciences*, *68*(10), 2236–2249. https://doi.org/10.1175/jas-d-10-05024.1

Emanuel, K., Sundararajan, R., & Williams, J. (2008). Hurricanes and global warming: Results from downscaling IPCC AR4 simulations. *Bulletin of the American Meteorological Society*, *89*(3), 347–368. https://doi.org/10.1175/bams-89-3-347

Franklin, J. L., Lord, S. J., Feuer, S. E., & Marks, F. D. (1993). The kinematic structure of hurricane Gloria (1985) determined from nested analyses of dropwindsonde and Doppler radar data. *Monthly Weather Review*, *121*(9), 2433–2451. https://doi.org/10.1175/1520-0493(1993)121<2433:tksohg>2.0.co;2

Gopalakrishnan, S. G., Marks, F., Zhang, X., Bao, J.-W., Yeh, K.-S., & Atlas, R. (2011). The experimental HWRF system: A study on the influence of horizontal resolution on the structure and intensity changes in tropical cyclones using an idealized framework. *Monthly Weather Review*, *139*(6), 1762–1784. https://doi.org/10.1175/2010mwr3535.1

Gori, A., Lin, N., & Smith, J. (2020). Assessing compound flooding from landfalling tropical cyclones on the North Carolina coast. *Water Resources Research*, *56*(4). https://doi.org/10.1029/2019wr026788

Gori, A., Lin, N., & Xi, D. (2020). Tropical cyclone compound flood hazard assessment: From investigating drivers to quantifying extreme water levels. *Earth's Future*, *8*(12). https://doi.org/10.1029/2020ef001660

Gori, A., Lin, N., Xi, D., & Emanuel, K. (2022). Tropical cyclone climatology change greatly exacerbates US extreme rainfall–surge hazard. *Nature Climate Change*, *12*(2), 171–178. https://doi.org/10.1038/s41558-021-01272-7

Harris, D. L. (1963). *Characteristics of the hurricane storm surge*. Department of Commerce. Retrieved from https://cds.climate.copernicus.eu/cdsapp#!/dataset/reanalysis-era5-pressure-levels-monthly-means?tab=overview

Hersbach, H., Bell, B., Berrisford, P., Biavati, G., Horányi, A., Muñoz Sabater, J., et al. (2018). ERA5 monthly mean data on pressure levels from 1979 to present [Dataset]. Chang. https://doi.org/10.24381/cds.bd0915c6

Hersbach, H., Bell, B., Berrisford, P., Hirahara, S., Horányi, A., Muñoz-Sabater, J., et al. (2020). The ERA5 global reanalysis. *Quarterly Journal of the Royal Meteorological Society*, *146*(730), 1999–2049. https://doi.org/10.1002/qj.3803

Holland, G. J. (1980). An analytic model of the wind and pressure profiles in hurricanes. *Monthly Weather Review*, *108*(8), 1212–1218. https://doi.org/10.1175/1520-0493(1980)108<1212:aamotw>2.0.co;2

Holland, G. J. (2008). A revised hurricane pressure–wind model. *Monthly Weather Review*, *136*(9), 3432–3445. https://doi.org/10.1175/2008mwr2395.1

Holland, G. J., Belanger, J. I., & Fritz, A. (2010). A revised model for radial profiles of hurricane winds. *Monthly Weather Review*, *138*(12), 4393–4401. https://doi.org/10.1175/2010mwr3317.1

Hu, K., Chen, Q., & Kimball, S. K. (2012). Consistency in hurricane surface wind forecasting: An improved parametric model. *Natural Hazards*, *61*(3), 1029–1050. https://doi.org/10.1007/s11069-011-9960-z

Irish, J. L., Resio, D. T., & Ratcliff, J. J. (2008). The influence of storm size on hurricane surge. *Journal of Physical Oceanography*, *38*(9), 2003–2013. https://doi.org/10.1175/2008jpo3727.1

Jing, R., & Lin, N. (2020). An environment-dependent probabilistic tropical cyclone model. *Journal of Advances in Modeling Earth Systems*, *12*(3), 1–18. https://doi.org/10.1029/2019ms001975

Joyce, B. R., Gonzalez-Lopez, J., Van der Westhuysen, A. J., Yang, D., Pringle, W. J., Westerink, J. J., & Cox, A. T. (2019). U.S. IOOS coastal and ocean modeling testbed: Hurricane-induced winds, waves, and surge for deep ocean, reef-fringed islands in the Caribbean. *Journal of Geophysical Research: Oceans*, *124*(4), 2876–2907. https://doi.org/10.1029/2018jc014687

Klotz, B. W., & Jiang, H. (2016). Global composites of surface wind speeds in tropical cyclones based on a 12 year scatterometer database. *Geophysical Research Letters*, *43*(19), 480–488. https://doi.org/10.1002/2016gl071066

Klotz, B. W., & Jiang, H. (2017). Examination of surface wind asymmetries in tropical cyclones. Part I: General structure and wind shear impacts. *Monthly Weather Review*, *145*(10), 3989–4009. https://doi.org/10.1175/mwr-d-17-0019.1

Klotzbach, P. P. J., Bowen, S. G., Pielke, R. G. R., & Bell, M. (2018). Continental U.S. hurricane landfall frequency and associated damage: Observations and future risks. *Bulletin of the American Meteorological Society*, *99*(7), 1359–1376. https://doi.org/10.1175/bams-d-17-0184.1

Landsea, C. W., & Franklin, J. L. (2013a). Atlantic hurricane database uncertainty and presentation of a new database format. *Monthly Weather Review*, *141*(10), 3576–3592. https://doi.org/10.1175/mwr-d-12-00254.1

Landsea, C. W., & Franklin, J. L. (2013b). Atlantic hurricane database uncertainty and presentation of a new database format. [Dataset]. National Hurricane Center. Retrieved from https://www.nhc.noaa.gov/data/%23hurdat

Lee, C.-Y., Camargo, S. J., Sobel, A. H., & Tippett, M. K. (2020). Statistical–dynamical downscaling projections of tropical cyclone activity in a warming climate: Two diverging Genesis scenarios. *Journal of Climate*, *33*(11), 4815–4834. https://doi.org/10.1175/jcli-d-19-0452.1

Lee, C.-Y., Tippett, M. K., Sobel, A. H., & Camargo, S. J. (2018). An environmentally forced tropical cyclone hazard model. *Journal of Advances in Modeling Earth Systems*, *10*(1), 223–241. https://doi.org/10.1002/2017ms001186

Lin, N., & Chavas, D. (2012). On hurricane parametric wind and applications in storm surge modeling. *Journal of Geophysical Research*, *117*(9), 1–19. https://doi.org/10.1029/2011jd017126

Lin, N., Emanuel, K. A., Smith, J. A., & Vanmarcke, E. (2010). Risk assessment of hurricane storm surge for New York City. *Journal of Geophysical Research*, *115*(18), 1–11. https://doi.org/10.1029/2009jd013630

Lin, N., Smith, J. A., Villarini, G., Marchok, T. P., & Baeck, M. L. (2010). Modeling extreme rainfall, winds, and surge from Hurricane Isabel (2003). *Weather and Forecasting*, *25*(5), 1342–1361. https://doi.org/10.1175/2010waf2222349.1

Lu, P., Lin, N., Emanuel, K., Chavas, D., & Smith, J. (2018). Assessing hurricane rainfall mechanisms using a physics-based model: Hurricanes Isabel (2003) and Irene (2011). *Journal of the Atmospheric Sciences*, *75*(7), 2337–2358. https://doi.org/10.1175/jas-d-17-0264.1

Luettich, R. A., & Westerink, J. J. (2018). ADCIRC users' manual V53.

Luettich, R. A., Westerink, J. J., & Scheffner, N. W. (1992). ADCIRC: An advanced three-dimensional circulation model for shelves, coasts, and estuaries. *Report 1, Theory and methodology of ADCIRC-2DD1 and ADCIRC-3DL.*

Marks, F. D., Houze, R. A., & Gamache, J. F. (1992). Dual-aircraft investigation of the inner core of hurricane Norbert. Part I: Kinematic structure. *Journal of the Atmospheric Sciences*, *49*(11), 919–942. https://doi.org/10.1175/1520-0469(1992)049<0919:daioti>2.0.co;2

21698996, 2022, 17, Downloaded from https://agupubs.onlinelibrary.wiley.com/doi/10.1029/2021JD036359, Wiley Online Library on [20/12/2023]. See the Terms and Conditions (https://onlinelibrary.wiley.com/terms-and-conditions) on Wiley Online Library for rules of use; OA articles are governed by the applicable Creative Commons License

Marsooli, R., & Lin, N. (2018). Numerical modeling of historical storm tides and waves and their interactions along the U.S. East and Gulf Coasts. *Journal of Geophysical Research: Oceans*, *123*(5), 3844–3874. https://doi.org/10.1029/2017jc013434

Marsooli, R., Lin, N., Emanuel, K., & Feng, K. (2019). Climate change exacerbates hurricane flood hazards along US Atlantic and Gulf Coasts in spatially varying patterns. *Nature Communications*, *10*(1), 1–9. https://doi.org/10.1038/s41467-019-11755-z

Mayo, T., & Lin, N. (2019). The effect of the surface wind field representation in the operational storm surge model of the National Hurricane Center. *Atmosphere*, *10*(4), 13–16. https://doi.org/10.3390/atmos10040193

Olfateh, M., Callaghan, D. P., Nielsen, P., & Baldock, T. E. (2017). Tropical cyclone wind field asymmetry-Development and evaluation of a new parametric model. *Journal of Geophysical Research: Oceans*, *122*(1), 458–469. https://doi.org/10.1002/2016jc012237

Pielke, R. A., Gratz, J., Landsea, C. W., Collins, D., Saunders, M. A., & Musulin, R. (2008). Normalized hurricane damage in the United States: 1900–2005. *Natural Hazards Review*, *9*(1), 29–42. https://doi.org/10.1061/(asce)1527-6988(2008)9:1(29)

Powell, M., Houston, S. H., Amat, L. R., & Morisseau-Leroy, N. (1998a). The HRD real-time hurricane wind analysis system. *Journal of Wind Engineering and Industrial Aerodynamics*, *77–78*, 53–64. https://doi.org/10.1016/s0167-6105(98)00131-7

Powell, M., Houston, S. H., Amat, L. R., & Morisseau-Leroy, N. (1998b). The HWind data of hurricanes [Dataset]. HWind Legacy Archive. Retrieved from https://www.rms.com/event-response/hwind/legacy-archive/

Powell, M., & Reinhold, T. A. (2007). Tropical cyclone destructive potential by integrated kinetic energy. *Bulletin of the American Meteorological Society*, *88*(4), 513–526. https://doi.org/10.1175/bams-88-4-513

Rappaport, E. N. (2014). Fatalities in the United States from Atlantic tropical cyclones: New data and interpretation. *Bulletin of the American Meteorological Society*, *95*(3), 341–346. https://doi.org/10.1175/bams-d-12-00074.1

Rego, J. L., & Li, C. (2009). On the importance of the forward speed of hurricanes in storm surge forecasting: A numerical study. *Geophysical Research Letters*, *36*(7), 1–5. https://doi.org/10.1029/2008gl036953

Resio, D. T., & Westerink, J. J. (2008). Modeling the physics of storm surges. *Physics Today*, *61*(9), 33–38. https://doi.org/10.1063/1.2982120

Sampson, C. R., Goerss, J. S., Knaff, J. A., Strahl, B. R., Fukada, E. M., & Serra, E. A. (2018). Tropical cyclone gale wind radii estimates, forecasts, and error forecasts for the Western North Pacific. *Weather and Forecasting*, *33*(4), 1081–1092. https://doi.org/10.1175/waf-d-17-0153.1

Shapiro, L. J. (1983). The asymmetric boundary layer flow under a translating hurricane. *Journal of the Atmospheric Sciences*, *40*(8), 1984–1998. https://doi.org/10.1175/1520-0469(1983)040<1984:tablfu>2.0.co;2

Thomas, A., Dietrich, J. C., Asher, T. G., Bell, M., Blanton, B. O., Copeland, J. H., et al. (2019). Influence of storm timing and forward speed on tides and storm surge during Hurricane Matthew. *Ocean Modelling*, *137*, 1–19. https://doi.org/10.1016/j.ocemod.2019.03.004

Thomsen, G. L., Smith, R. K., & Montgomery, M. T. (2015). Tropical cyclone flow asymmetries induced by a uniform flow revisited. *Journal of Advances in Modeling Earth Systems*, *7*(3), 1265–1284. https://doi.org/10.1002/2015ms000477

Torres, M. J., Reza Hashemi, M., Hayward, S., Spaulding, M., Ginis, I., & Grilli, S. T. (2019). Role of hurricane wind models in accurate simulation of storm surge and waves. *Journal of Waterway, Port, Coastal, and Ocean Engineering*, *145*(1), 04018039. https://doi.org/10.1061/(asce)ww.1943-5460.0000496

Ueno, M., & Bessho, K. (2011). A statistical analysis of near-core surface wind asymmetries in typhoons obtained from QuikSCAT data. *Journal of the Meteorological Society of Japan*, *89*(3), 225–241. https://doi.org/10.2151/jmsj.2011-304

Uhlhorn, E. W., Klotz, B. W., Vukicevic, T., Reasor, P. D., & Rogers, R. F. (2014). Observed hurricane wind speed asymmetries and relationships to motion and environmental shear. *Monthly Weather Review*, *142*(3), 1290–1311. https://doi.org/10.1175/mwr-d-13-00249.1

Vijayan, L., Huang, W., Yin, K., Ozguven, E., Burns, S., & Ghorbanzadeh, M. (2021). Evaluation of parametric wind models for more accurate modeling of storm surge: A case study of hurricane Michael. *Natural Hazards*, *106*(3), 2003–2024. https://doi.org/10.1007/s11069-021-04525-y

Wang, S., & Toumi, R. (2016). On the relationship between hurricane cost and the integrated wind profile. *Environmental Research Letters*, *11*(11), 114005. https://doi.org/10.1088/1748-9326/11/11/114005

Wang, S., & Toumi, R. (2021). Recent tropical cyclone changes inferred from ocean surface temperature cold wakes. *Scientific Reports*, *11*(1), 22269. https://doi.org/10.1038/s41598-021-01612-9

Wang, S., Toumi, R., Czaja, A., & Kan, A. V. (2015). An analytic model of tropical cyclone wind profiles. *Quarterly Journal of the Royal Meteorological Society*, *141*(693), 3018–3029. https://doi.org/10.1002/qj.2586

Wang, S., Toumi, R., Ye, Q., Ke, Q., Bricker, J., Tian, Z., & Sun, L. (2021). Is the tropical cyclone surge in Shanghai more sensitive to landfall location or intensity change? *Atmospheric Science Letters*, *22*(10), 1–8. https://doi.org/10.1002/asl.1058

Wang, Y., Rao, Y., Tan, Z.-M., & Schönemann, D. (2015). A statistical analysis of the effects of vertical wind shear on tropical cyclone intensity change over the Western North Pacific. *Monthly Weather Review*, *143*(9), 3434–3453. https://doi.org/10.1175/mwr-d-15-0049.1

Weisberg, R. H., & Zheng, L. (2006). Hurricane storm surge simulations for Tampa Bay. *Estuaries and Coasts*, *29*(6), 899–913. https://doi.org/10.1007/bf02798649

Willmott, C. J. (1981). On the validation of models. *Physical Geography*, *2*(2), 184–194. https://doi.org/10.1080/02723646.1981.10642213

Willoughby, H. E., Darling, R. W. R., & Rahn, M. E. (2006). Parametric representation of the primary hurricane vortex. Part II: A new family of sectionally continuous profiles. *Monthly Weather Review*, *134*(4), 1102–1120. https://doi.org/10.1175/mwr3106.1

Wong, B., & Toumi, R. (2016). Effect of extreme ocean precipitation on sea surface elevation and storm surges. *Quarterly Journal of the Royal Meteorological Society*, *142*(699), 2541–2550. https://doi.org/10.1002/qj.2845

Xi, D., Lin, N., & Smith, J. (2020). Evaluation of a physics-based tropical cyclone rainfall model for risk assessment. *Journal of Hydrometeorology*, *21*(9), 2197–2218. https://doi.org/10.1175/jhm-d-20-0035.1

Xu, H., Lin, N., Huang, M., & Lou, W. (2020). Design tropical cyclone wind speed when considering climate change. *Journal of Structural Engineering*, *146*(5), 04020063. https://doi.org/10.1061/(asce)st.1943-541x.0002585

Yin, J., Jonkman, S., Lin, N., Yu, D., Aerts, J., Wilby, R., et al. (2020). Flood risks in sinking delta cities: Time for a reevaluation? *Earth's Future*, *8*(8). https://doi.org/10.1029/2020ef001614

Zhang, X., Gopalakrishnan, S. G., Trahan, S., Quirino, T. S., Liu, Q., Zhang, Z., et al. (2016). Representing multiple scales in the Hurricane Weather Research and forecasting modeling system: Design of multiple sets of movable multilevel nesting and the basin-scale HWRF forecast application. *Weather and Forecasting*, *31*(6), 2019–2034. https://doi.org/10.1175/waf-d-16-0087.1

Zhu, L., Quiring, S. M., & Emanuel, K. A. (2013). Estimating tropical cyclone precipitation risk in Texas. *Geophysical Research Letters*, *40*(23), 6225–6230. https://doi.org/10.1002/2013gl058284

21698996, 2022, 17, Downloaded from https://agupubs.onlinelibrary.wiley.com/doi/10.1029/2021JD036359, Wiley Online Library on [20/12/2023]. See the Terms and Conditions (https://onlinelibrary.wiley.com/terms-and-conditions) on Wiley Online Library for rules of use; OA articles are governed by the applicable Creative Commons License